



UKAEA-CCFE-PR(25)360

C. L. MacLean, M. Cecconello, S. Allan, C. L. Grove, R. Worrall, the MAST Upgrade Team

Absolute neutron emission estimate on MAST Upgrade based on activation foil measurements

Enquiries about copyright and reproduction should in the first instance be addressed to the UKAEA Publications Officer, Culham Science Centre, Building K1/0/83 Abingdon, Oxfordshire, OX14 3DB, UK. The United Kingdom Atomic Energy Authority is the copyright holder.
The contents of this document and all other UKAEA Preprints, Reports and Conference Papers are available to view online free at scientific-publications.ukaea.uk/

Absolute neutron emission estimate on MAST Upgrade based on activation foil measurements

C. L. MacLean, M. Cecconello, S. Allan, C. L. Grove, R. Worrall, the MAST Upgrade Team

Absolute neutron emission estimate on MAST Upgrade based on activation foil measurements

C. L. MacLean¹, M. Cecconello^{1,2}, S. Allan³, C. L. Grove³, R. Worrall³ and the MAST Upgrade Team[‡]

- ¹ Department of Physics, University of Durham, DH1 3LS, United Kingdom
- 2 Department of Physics and Astronomy, Uppsala University, Uppsala SE-75105, Sweden.
- 3 United Kingdom Atomic Energy Authority, Culham Campus, Abingdon,
Oxon, OX14 3DB, United Kingdom

E-mail: craig.l.maclean@durham.ac.uk

August 2024

Abstract. Determination of the absolute neutron rate production in any fusion device and in particular for ITER and future power plants is essential for their operation and for the optimization of the fusion power. A common calibration approach is to use a well characterized neutron sources placed inside the vacuum vessel combined with Monte Carlo simulations. This method is fraught with several difficulties both from an engineering and data modeling and interpretation point of view. This is particularly true for future fusion power plants. This work demonstrate an alternative approach to the absolute calibration of the neutron rate based on activation foil measurements combined with forward modeling of a well characterized plasma discharge and fusion device. This method has been applied to MAST Upgrade and the good agreement found between measured and modeled foil activity support this approach. The results presented suffer from some limitation but suggestions are given on how to resolve them.

1. Introduction

Absolute calibration of neutron diagnostics is fundamental for the safe operation of present day devices and future power plant reactors and for the estimates of the total fusion power. The most commonly used approach is to monitor the neutron emission with absolutely calibrated fission chamber using a strong neutron source with a well characterized neutron emission spectrum placed at different locations inside the vacuum vessel [1, 2, 3, 4, 5, 6, 7, 8, 9]. Neutron transport Monte Carlo codes are then used to model the neutron source, the tokamak and its environment and the FC thus providing the relationship between the neutron source strength and the measured flux at the absolutely calibrated FC [10, 11]. This method, however, is technologically quite complex and time consuming (with long shut-down periods) requiring in addition very strong neutron sources with the associated complications for their safe handling. In addition, periodic calibration are required to track changes in the calibration factors. Activation foil measurements are often used as additional benchmarks of this calibration method and good agreement between the two has been

† See author list of J. Harrison, et al. 2019 Nucl. Fusion 59 11201

reported extensively in literature [12, 13, 14, 15, 16]. An alternative approach is the use of well characterized plasma discharges as the neutron source in combination with neutron Activation Foils (AFs), located in the proximity of the plasma. The neutron source is modeled by codes such as TRANSP/NUBEAM [17, 18] while the total neutron flux at the AF location which includes scattered neutrons is calculated via neutron transport Monte Carlo codes. Agreement between predicted and observed activation is then used to confirm the correctness of the modeling and to provide the absolute calibration factors for the fission chambers. Although this approach is also based on neutron transport calculation, the modeling effort is quite reduced if the AFs are placed inside the vacuum vessel and as close as possible to the neutron source. This also ensures that the total neutron field at the AF locations is not significantly affected by changes in the environment outside the tokamak which is not uncommon during the typical life-time of a fusion device. This second approach to the absolute neutron calibration as applied to MAST Upgrade is described in this work. MAST Upgrade is a spherical tokamak with a large aspect ratio $R/a \approx 0.85/0.65 \approx 1.3$ operated with low magnetic field (typically between 0.4 and 0.7 T) and plasma currents in the range 0.5 - 1.0 MA. External auxiliary heating is currently provided by two Neutral Beam Injection (NBI) system delivering up to 3.5 MW of heating power by injecting deuterons with energies up to 70 keV (two additional NBIs are planned to be installed in the near future). Neutron emission on MAST Upgrade is entirely dominated by the beam-thermal ($\approx 85\%$) and beam-beam ($\approx 15\%$) fusion reactions with the thermal contribution being negligible. MAST Upgrade is equipped with three neutron diagnostics: a set of two fission chambers located outside and in close proximity to the vacuum vessel, an absolutely calibrated neutron camera (NCU, [19, 20]) and three activation foil stations. While the fission chambers and the neutron camera are standard diagnostic always available, the activation stations are used only on a limited number of experimental dates. Section 2 details the properties of the activation stations, of the activation foils and of the γ -rays detectors used to measure the activity as well as the experimental dates on which AF measurements were collected. The modeling of the neutron flux at the AF locations and expected number of counts on the γ -rays detectors for these experimental dates are presented in section 3 together with the error analysis. The comparison between predicted and measured counts and the implications for the absolute calibration of fission chambers is discussed in section 4 where also the conclusions are drawn.

2. Experimental setup

MAST Upgrade is equipped with three activation foil stations located in sectors 5, 10 and 12 around the machine at (R,Z)=(202,-11) cm, (R,Z)=(202,-21) cm and (R,Z)=(202,10) cm respectively. Each station consists of a re-entrant pipe mounted on the equatorial flange and separated by the vacuum chamber by a thin wall of 0.7 mm thickness to reduce the absorption and scattering of neutrons. A CAD view of activation stations at sectors 5 and 12 are shown in figure 1. The activation foil disks are placed inside a hollow plastic cylinder which is manually inserted into the re-entrant pipe at the beginning of each experimental day. A view of the activation foil location from inside the vessel is shown in figure 2. Four identical Indium disks were used each with a diameter of 25 mm and a thickness of 4 mm with an assumed natural isotopic fraction of 95.71 % for 115 In and 4.29 % for 113 In (no certification was available). Activation foils measurements were carried out parasitically on a number

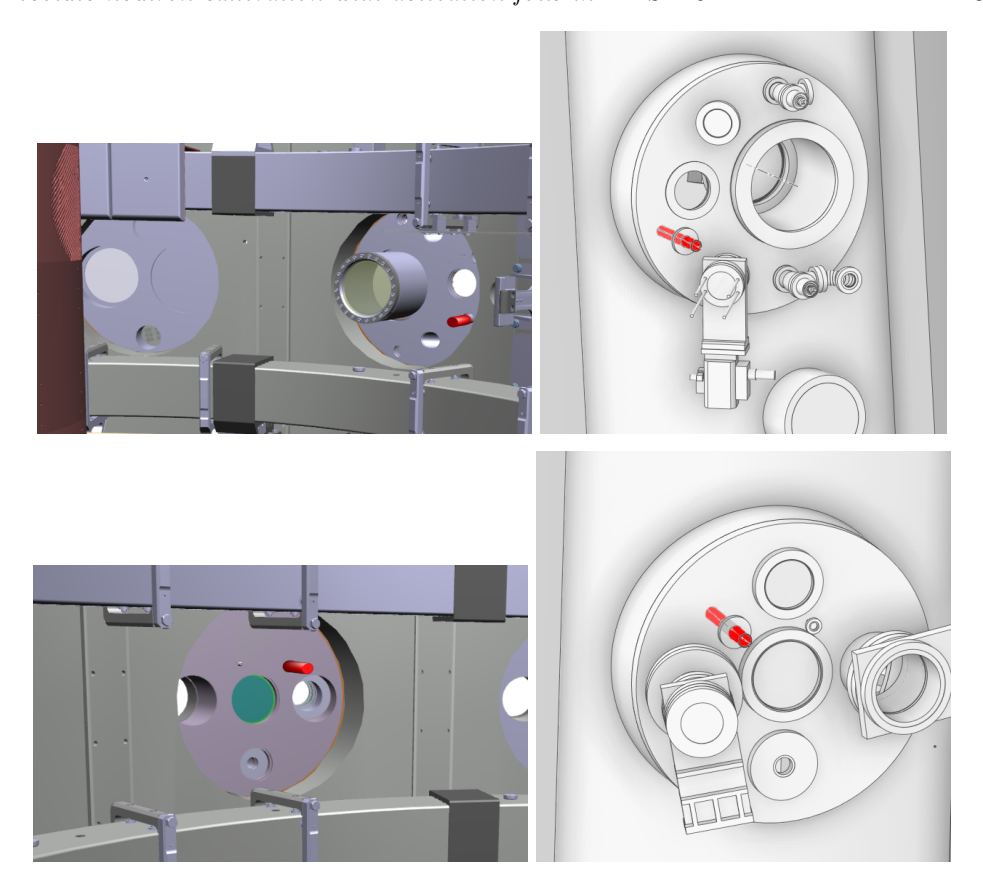


Figure 1 – CAD view of the activation foil stations (in red) in sectors 5 (top) and 12 (bottom) on the equatorial flanges from the inside/outside of the vacuum vessel (on the left)/right respectively). Clearly visible in the view from the inside are the P5 upper and lower poloidal field coils.

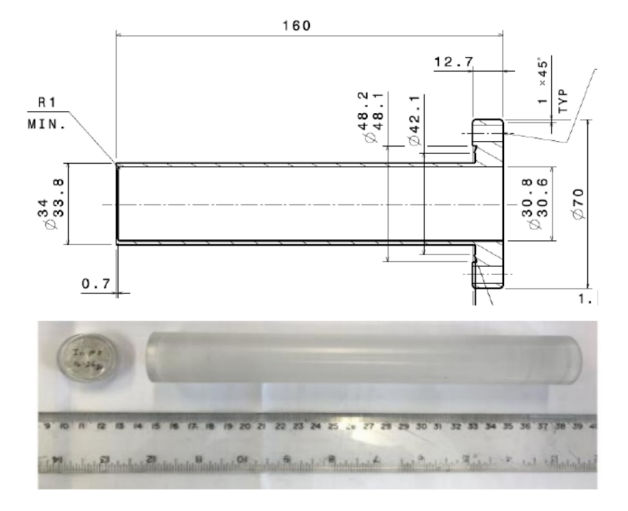


Figure 2 – CAD cross-section of an activation foil re-entrant flange (top) and a phot of the activation foil with plastic sleeve for insertion and removal.

Table 1 – Complete list of the AF measurements carried out during the MAST Upgrade experimental campaigns MU01 to MU03. Columns: γ -ray detector (B for BEGe, S for SAGe); fission chamber fluence; experimentally measured number of decays $N_{\rm E}$ and specific activity $A_{\rm S}$ after each experimental day and total number of counts on the Neutron Camera Upgrade (NCU).

Exp.	Date	Sector	γ	Fluence	$N_{ m E}$	A_{S}	NCU	Pulse
Camp.		and AF		$(\times 10^{14})$	$(\times 10^5)$	(Bq/g)	$(\times 10^6)$	numbers
MU01	08-10-21	12/7	В	1.02	1.740	15 ± 1	1.45	45212-45221
	15-10-21	12/7	В	1.50	0.154	17 ± 1	-	45302-45316
	22-10-21	12/6	В	2.12	3.227	27 ± 2	2.79	45392-45401
	28-10-21	12/7	В	2.51	0.137	16 ± 1	1.75	45474, 45483
MU02	26-01-23	12/4	В	1.99	2.942	40 ± 4	3.05	47078-47097
	27-01-23	12/7	В	1.90	1.952	26 ± 2	-	47101-47119
MU03	20-10-23	5/7	В	1.44	2.196	25 ± 2	2.03	48543-48547
		12/8	S		1.541	25 ± 2		
	27-10-23	5/4	В	1.22	4.026	42 ± 3	5.02	48609-48624
		12/8	S		2.786	42 ± 3		
	19-12-23	12/8	В	2.76	3.001	30 ± 2	-	49186-49200
		5/7	S		2.928	42 ± 3		
	18-01-24	5/7	В	3.21	3.749	39 ± 3	4.85	49363-49379
		12/8	S		3.678	57 ± 5		

of experimental days during the first three MAST Upgrade scientific campaigns (indicated as MU01, MU02, and MU03 respectively) and are listed in table 1. These consisted of a large variety of (i) plasma scenarios with currents ranging from 0.6 to 1.0 MA in L- or H-mode, of (ii) NBI heating timing and combinations (on-axis only, off-axis only or both) of (iii) plasma density and temperature, of (iv) equilibria (singleand double-null conventional divertor or Super-X divertor) with (v) a broad spectrum of MHD instabilities (sawteeth, TAEs, fish-bones, Long-Lived Mode, Neoclassical Tearing Modes, ELMs, Internal Reconnection Events) and (vi) different ELM controls mechanisms. As a result, the spatial distribution and time evolution of the neutron emissivity varied significantly as shown in figure 3 where the time trace of the fission chamber for the experimental day on the 08-10-2021 is shown. The AFs were inserted prior to the first plasma discharge of each experimental day and removed after the last one. The start time of the irradiation sequence was set to zero at the start of the first NBI heating and the irradiation duration (i.e. the NBI heating time) was accurately recorded. The activity was measured immediately after the end of each experimental day for 24 hours (resulting in approximately 98% of nuclides on the activation foil having decayed). Two absolutely calibrated γ -rays detectors are used: a Broad Energy High-Purity Germanium HP-Ge BE3825 (BEGe) and a Single Anode Germanium (SAGe) well-type detector. Data acquisition was carried out via a Lynx digital MCA device connected to a PC with Genie 2000 software for analysis, again taking care of noting the start and end time of the activation measurements. An energy calibration and efficiency check were carried out with a Co-60 γ -rays source of known activity for each experimental day and background radiation checks were regularly done to ensure that the measurements were not contaminated by unwanted radiation sources. The typical dead-time observed during the activation measurements was less than 0.3 % of the counting time. The activated nuclide of interest is the metastable state of In-115m with half-life 4.49 hours which, after irradiation from a 2.45

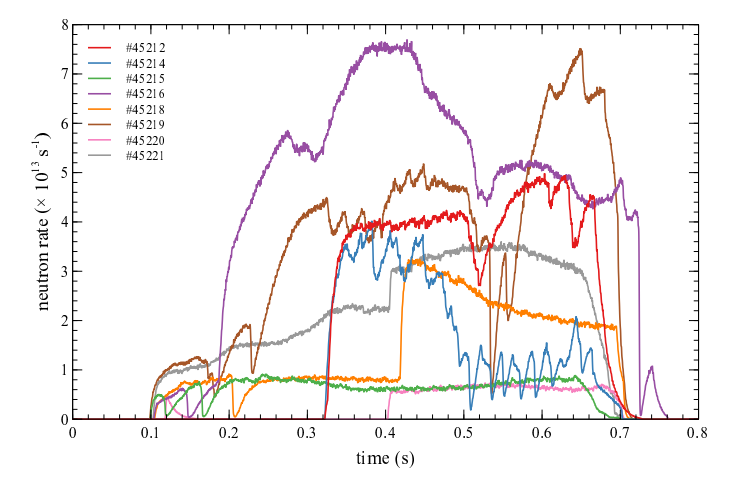


Figure 3 – Time evolution of the neutron rate measured by the fission chamber for the activation foil measurement on the 08-10-2021.

MeV neutrons, emits a γ -ray with energy $E_{\gamma} = 336$ keV together with several delayed γ -rays from induced neutron capture in the AF. The absolute efficiency ϵ at $E_{\gamma}=336$ keV is $0.0762 \pm 8\%$ and $0.0539 \pm 8\%$ for the BEGe and SAGe detectors respectively. This has been estimated numerically using the Canberra LabSOCS software which is based on the simulation of the γ -ray energy spectrum for a known source and detector combination using the Monte Carlo transport code MCNP [21] verified against known measurements. An example of the γ -rays energy spectrum emitted by the activated In foil after the exposure to MAST-U on the 08-10-2021 is shown in figure 4 with the insert showing the photo-peak of the 336.35 keV γ -ray emitted by the first meta-stable In foil with a branching ratio of 0.95. The red area represent the actual counts with the radiation background subtracted. The specific activity, the neutron fluence measured by the fission chamber and the total neutron counts measured by the neutron camera (the integral of the sum of the count rates in each of the six lines of sight) are reported in table 1. Neutron camera data were not available for all the activation measurements as indicated in the table. The relationship between the neutron fluence and the specific activity is shown in the left panel of figure 5: although roughly proportional to each other, there are some large deviations from a purely linear relationship. The right panel of the same figure shows the relationship between the neutron fluence as measured by the fission chamber and the total neutron counts obtained from the NCU: the very good linear relationship between the two indicates that the large deviations from the expected linearity in the case of the specific activity can not be attributed to problems in the fission chamber. Note that the NCU is absolutely calibrated while the fission chamber is not. Instead the FC has been matched to TRANSP/NUBEAM predictions in selected plasma scenarios characterized by no fast ion losses or redistribution as inferred from the absence of the typical signature in the OMAHA Mirnov pick-up coils of MHD instabilities such as TAEs, FBs, LLMs, sawteeth and ELMs. A detail analysis of the AF measurements has shown no clear dependency on the specific foil, the measurement location (sector), the experimental campaign and the γ -rays detector used. The reason for this behavior remains unclear to date.

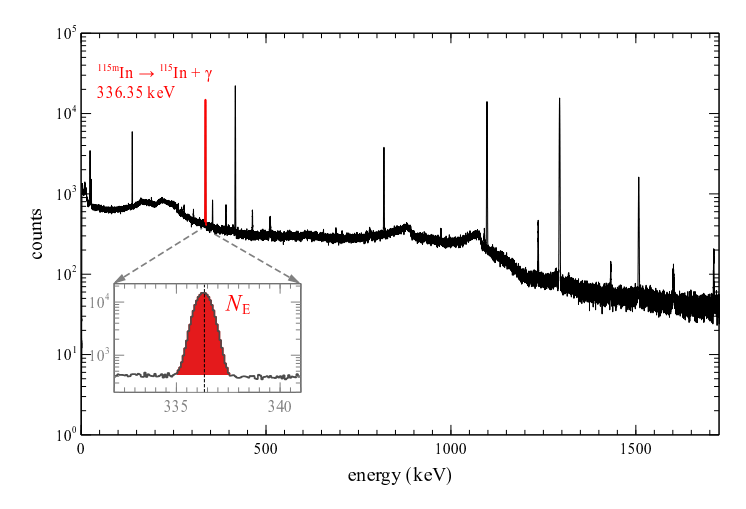


Figure 4 – Energy spectra collected for 24 hours from the BEGe detector of the activation foil 7 in sector 12 after its exposure to MAST-U plasmas on the 08-10-2021. The red peak corresponds to experimental counts $N_{\rm E}$ of the 336 keV gammas produced from the decay of activated $^{115m}{\rm In}$. All the other main peaks in the spectrum are due to the delayed γ -rays emission following neutron capture in the foil.

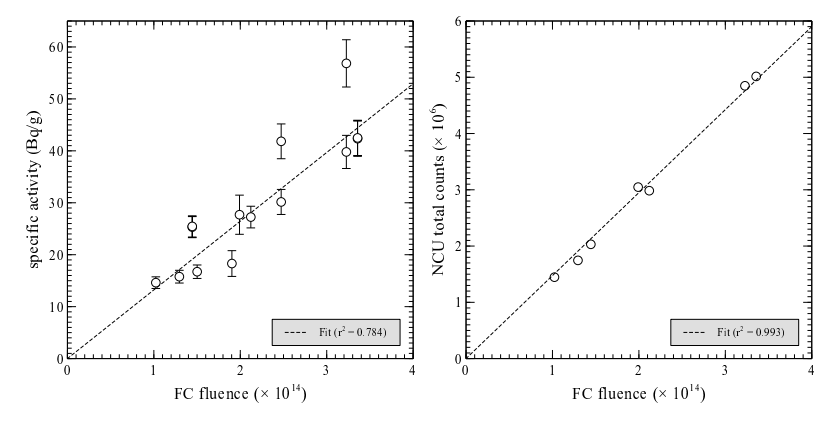


Figure 5 – Scaling between the neutron fluence as measured by the fission chamber and the specific activity (left panel) of the AFs and the NCU total counts (right panel) for all AF experiments.

3. Modeling of the induced activity in the ¹¹⁵In foil

Modeling of the induced activity in the 115 In foils requires the estimation of the neutron flux on the foil including both the direct and scattered neutron contributions during each plasma discharge, the modeling of the irradiation and decay sequence for the entire exposure day and the modeling of the detection of the γ -rays during the activity measurements. This will provide the predicted number of counts expected in the 336 keV γ -ray peak which will then be compared to the experimental observations reported in table 1. The neutron emissivity is calculated using the TRANSP/NUBEAM codes to estimate the direct neutron component and the MCNP code for the scattered one:

these two steps are detailed in sections 3.1 and 3.2 respectively. The neutron flux at the activation foil is calculated as described in section 3.3. Modeling of the irradiation and decay sequence and the expected γ -rays counts in the detector are described in section 3.4. Given the complexity of the steps involved only a limited number of days per experimental campaign were selected for the complete modeling: 08-10-2021 for MU01, 20-10-2023 and 27-10-2023 for MU03 and both days for MU02. The reason to select these pulses is that they provide a good representation of the spread in the experimentally measured specific activity around the expected linear relation.

3.1. TRANSP/NUBEAM modeling of the direct neutron emissivity

Each plasma discharge (indicated by the index q) has been modeled in TRANSP/NUBEAM using an externally imposed equilibrium calculated by EFIT++ constrained, whenever available, by measurements of the current density obtained via the motional Stark effect diagnostic [22]. The internal equilibrium solver (TEQ) was not used. Kinetic profiles were provided by the Thomson scattering diagnostic [23], while plasma rotation from CXRS spectroscopic diagnostic. No $Z_{\rm eff}$ measurement is available on MAST Upgrade and it was assumed to have a constant profile with the value of $Z_{\rm eff} = 1.5$. The fast ion distribution has been calculated by NUBEAM with high statistics including the correction for finite Larmor effects to account for the guiding-centre approximation in the calculation of the fast ion orbits. The NBIs energy fractions were set to their nominal values (0.70/0.19/0.11) for on-axis, 0.78/0.16/0.06for off-axis) with the exclusion of the on-axis NBI during MU01 which was set to 0.4/0.4/0.2 as inferred from spectroscopic measurements: this was due to an improper set-up of the magnets in the NBI ionization source that was rectified at the end of MU01. The non-flux averaged neutron emissivity has been calculated in 5 ms time intervals at M time points during the flat-top phase of each plasma discharge q. The non-flux averaged neutron emissivity is a more realistic representation of the neutron emissivity taking into account poloidal asymmetries that are neglected in the standard TRANSP/NUBEAM output. The non-flux neutron emissivity is calculated on an 2D irregular grid consisting of I = 840 points of coordinates (R_i, Z_i) to which a toroidal volume V_i and neutron emissivity ε_i are associated as shown in figure 6. Toroidal field ripples have a negligible effect on the confinement of fast ions [24] and they have not been included in the modeling. The reduced fast ion confinement due to MHD instabilities such internal reconnection events, sawteeth, TAEs, fish-bones, ELMS and to mode-locking can result in a significant reduction in the neutron emissivity and consequently of the neutron flux reaching the activation foil. The TRANSP/NUBEAM simplified models for sawtooth and fish-bones and the anomalous fast ion diffusion coefficient for the heuristic description of the effect of TAEs and LLMs have not been used in these simulations: the need of an ad-hoc adjustment of the several parameters in such models for each plasma discharge made this approach impractical. Instead, the neutron rate predicted by TRANSP/NUBEAM is compared to the one measured by the FC and scaled to match it: this correction factor, calculated as the ratio of the neutron fluences and indicated Γ as in the remainder of the paper, is of the order of 10 % form most cases, and at most 25 % for a few selected cases. An example is provided in figure 7 where the time traces for plasma discharge #45216 (see table 1) are shown. An IRE occurring at approximately 150 ms into the discharge causes a drop in the neutron emissivity, while between 200 - 300 ms TAEs and between 300 - 500 ms LLM results in the suppression of the fast ion population; the fast ion population remains

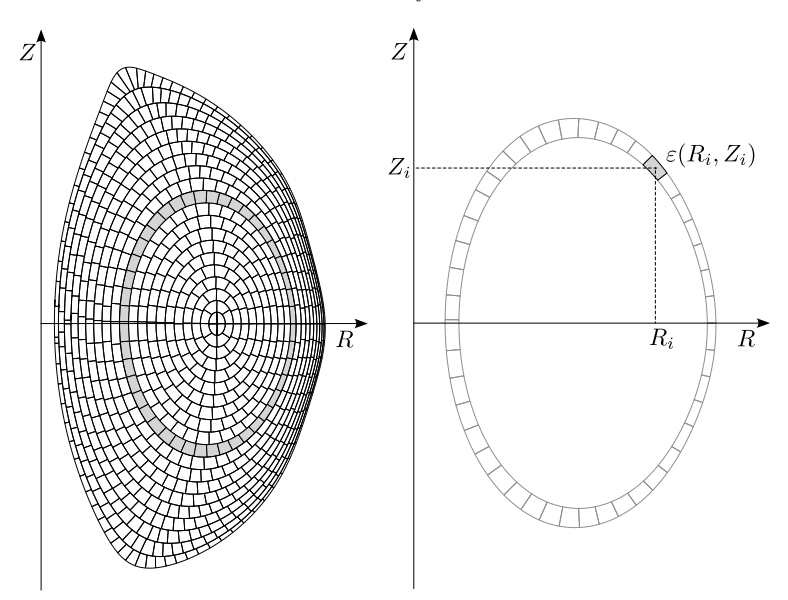


Figure 6 – Left figure: geometry of the 840 toroidally axis-symmetric zones used in TRANSP/NUBEAM in which the neutron emissivity ε is calculated for a typical MAST Upgrade equilibrium. The shaded region corresponds to the zones for a specific flux surface and it is shown in detail on the right where a single zone located at (R_i, Z_i) is shown with its non-flux averaged neutron emissivity $\varepsilon(R_i, Z_i)$.

below the TRANSP/NUBEAM prediction also during the mode-locking phase (from 500 ms to the end of the pulse). In this case the correction factor is $\Gamma = 0.795$.

3.2. MCNP modeling of the direct and scattered neutron flux

Due to the positioning of the activation foils, their proximity to the plasma and them directly facing the central column, the flux of scattered neutrons reaching them can be significant. In order to estimate the contribution of scattered neutrons to the total activation of the In foil, neutron transport calculations based on the Monte Carlo code MCNP were carried out. Three neutron sources have been used in these simulations representative of the typical neutron emissivity for off-axis only, on-axis only and both on- and off-axis NBI heating. The neutron source spatial distribution are based on the non-flux averaged neutron emissivity for three reference discharges: plasma discharge #45215 at 0.4 s for the off-axis case, #45216 at 0.4 s for both NBIs and #45219 at 0.35 s for on-axis NBI. For all the three cases, the neutron energy distribution from DD reactions has been assumed to be Gaussian centered at 2.45 MeV with a fullwidth at half maximum corresponding to a temperature of 70 keV which is equal the maximum injection energy of the NBIs in MAST-U. A 2D histogram of the spatial distribution of the MCNP neutron sources on the poloidal plane is shown in figure 8. The calculation of the direct and scattered neutron flux energy spectra were performed for all three activation foil locations (sector 5, 10 and 12) in the energy range 0 to 5 MeV. The special tally treatment provided by the INC keyword has been used to bin the number of collision per track with for those test particles crossing the surface of the cell representing the AF without having undergone any prior collision thus

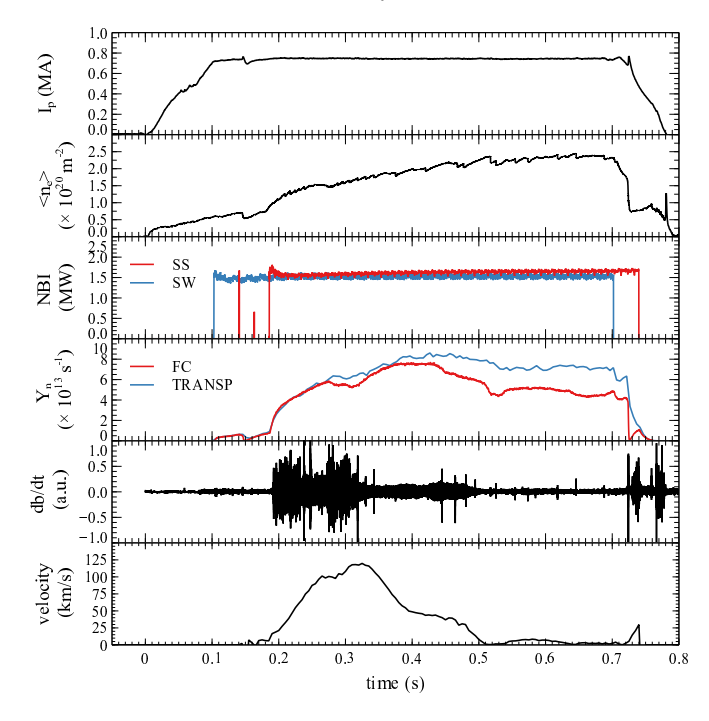


Figure 7 – Example (plasma discharge #45216) of how IRE (at 150 ms), TAEs (200 - 300 ms), LLM (300 - 500 ms) and mode-locking (after 500 ms) affect the neutron emissivity. From top to bottom: plasma current, line integrated electron density, on- and off-axis NBI power (SS and SW respectively), neutron rate from the FC (red) and TRANSP/NUBEAM (blue), magnetic fluctuation from OMAHA coils and plasma rotation in the core (around 1.0 m).

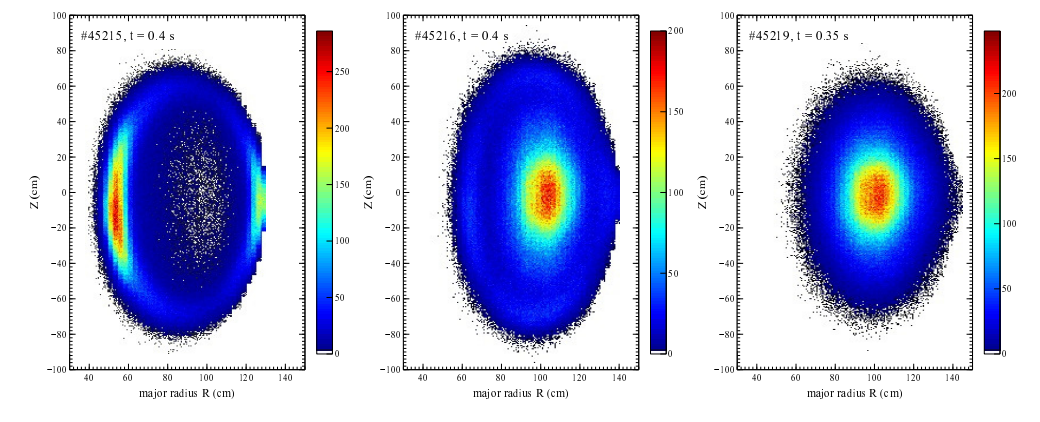


Figure 8 – 2D histogram of the sampled MCNP DD neutron sources in the poloidal plane with 10^6 markers and bin area of approximately 0.5×0.5 cm² for off-axis NBI only (#45215), both on- and off-axis NBIs (#45216) and on-axis NBI only (#45219). The colorbar indicated the number of markers in each bin.

giving the direct neutron flux per neutron Φ_D . The total neutron flux per neutron, Φ_T , was calculated using the standard F4 tally which, combined with the direct flux, allowed the estimation of the scattered neutrons flux $\Phi_S = \Phi_T - \Phi_D$. The histogram of the total, direct and scattered neutron fluxes in the 0 - 4 MeV range, in bins of 50 keV width, is shown in panels (a.1) and (b.1) of figure 9 for the activation foils at sector 10 for on-axis and off-axis only NBI. The results for sectors 5 and 12 are very similar to those obtained for sector 10. The broad Gaussian peak seen in figure 9 at an energy slightly below 2.45 MeV results from the superimposition of the scattered components of neutrons born with energies above 2.45 MeV. As shown in table 2, the

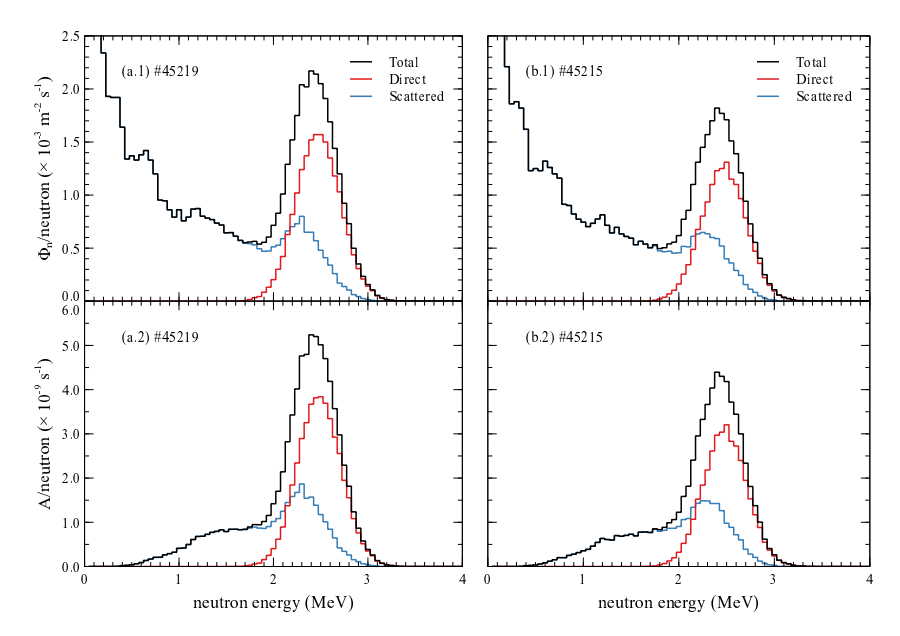


Figure 9 – Total (black), direct (red) and scattered (blue) neutron fluxes per simulated neutron Φ calculated by MCNP for the activation foil at sectors 10 for on- and off-axis only NBI heating (panels a.1 and b.1 respectively). Panels (a.2) and (b.2) show the corresponding activation rate per simulated neutron $A = \Sigma \Phi_n V$ where Σ is the inelastic macroscopic cross section for the ¹¹⁵In 1st meta-stable state and V the foil volume.

ratio $\int \Phi_{\rm S} dE/\int \Phi_{\rm D} dE$, where the integration is carried over the interval 0 to 5 MeV, is quite large for all sectors with the off-axis NBI only giving the largest values. The different components of the activation rate per simulated neutron $A = \Sigma \Phi V$, where Σ is the inelastic macroscopic cross section for the ¹¹⁵In first meta-stable state and V its volume, has been calculated and is shown in panels (a.2) and (b.2) of figure 9. As it can be seen the contribution of scattered neutrons to the total activation is not negligible. As described in section 3.1, from TRANSP/NUBEAM it is only possible to calculate the absolute direct neutron flux $\phi_{\rm D}$ at the activation foil (as described in section 3.3). The estimated total (direct plus scattered) neutron flux $\phi_{\rm T}$ is then calculated as $\phi_{\rm T} = \kappa \phi_{\rm D}$ where the constant κ is given by $\kappa = \int \Sigma \Phi_{\rm T} dE/\int \Sigma \Phi_{\rm D} dE$ and is reported in the last column of table 2 for the three reference scenarios. A comparison of κ for the off-axis only and on-axis only NBI scenarios shows that the scattered contribution is higher in the former as it can be expected since the source is stronger further away from the AF and closer to the central-column resulting in

a larger number of scattered neutrons. The values of κ for the on-axis only and with both NBIs are more similar since the neutron emissivity due to the off-axis NBI is approximately a factor 10 smaller than the one due to the on-axis NBI. Similar estimates were carried out for the PLT device where it was found that the activation by scattered neutrons was 1.24 times the one due to direct neutrons [25]. The reason for this value to be lower than the one reported here is that MAST Upgrade has a lower aspect ratio and a thinner central column $(R/a = 0.85/0.65 \approx 1.3)$ compared to PLT $(R/a = 1.3/0.4 \approx 3.3)$. As a consequence, each point on the first wall in MAST Upgrade (and hence the AF) sees a much larger neutron source volume and scattering surface.

Table 2 – Scattered and direct neutron flux per simulated neutron fractions estimated by MCNP at the location of the activation foils in Sectors 5, 10 and 12 together with the scattered to direct ratios and the scaling factor κ for on- and off-axis NBI heating used to calculate the absolute total flux on the activation foils.

Pulse	sector	$\int \Phi_{\rm S} dE / \int \Phi_{\rm T} dE$	$\int \Phi_{\rm D} dE / \int \Phi_{\rm T} dE$	$\int \Phi_{\rm S} dE / \int \Phi_{\rm D} dE$	κ
45215	5	0.77	0.23	3.43	1.81
off	10	0.79	0.21	3.78	1.92
axis	12	0.77	0.23	3.29	1.82
45216	5	0.76	0.24	3.17	1.76
on & off	10	0.78	0.22	3.51	1.87
axis	12	0.75	0.25	3.02	1.77
45219	5	0.75	0.25	3.00	1.74
on	10	0.76	0.24	3.20	1.81
axis	12	0.74	0.26	2.88	1.74

3.3. Total neutron flux and activation rate

For plasma discharge q, the direct neutron flux ϕ_D at the activation foil at time t_m is given by:

$$\phi_{D,q}(t_m) = \sum_{i=1}^{I} \sum_{j=1}^{J} \frac{n_i(t_m)}{S_{i,j}(t_m)}$$
(1)

where $n_i(t_m) = \varepsilon_i(t_m)\Delta V_i(t_m)$ is the rate of neutrons emitted isotropically by the fractional volume $\Delta V_i = V_i(t_m)/J$ over the entire solid angle and $S_{i,j}(t_m) = 4\pi d_{i,j}^2(t_m)$ is the surface of the sphere centered in $(R_i(t_m), Z_i(t_m), \varphi_j)$ at a distance $d_{i,j}$ from the activation foil. The effect of anisotropic neutron emission due to the dependence of the differential DD neutron production on the angle of emission is here neglected as its effect is to introduce variations less than 5 % [26]. The index i = 1...I runs over all the toroidal volumes while the index j = 1...J runs over the number J of fractional volumes ΔV_i in which each V_i is divided. Figure 10 shows the top view of the i-th toroidal volume (in blue) and the location of the activation foil (black dot): a fractional volume is shown in purple. The central column is also shown (light gray): the contribution to $\phi_{D,q}(t_m)$ from the fractional volumes that do not have a direct view of the AF (indicated in dark blue) is set to zero. The direct flux at the activation foil as a function of the toroidal angle is shown in figure 11 with and without the shadowing effect of the central column included. For each plasma discharge q, a single

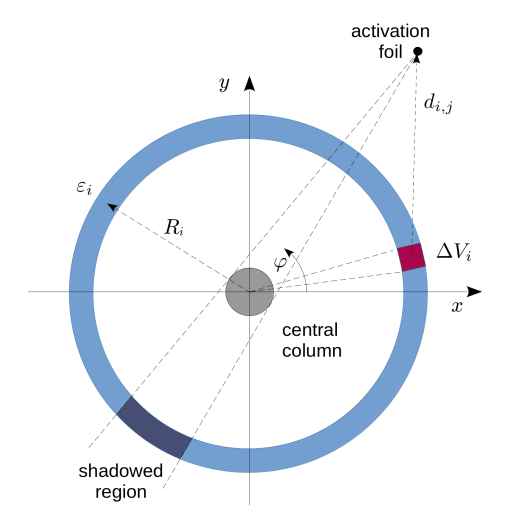


Figure 10 – Geometry used to calculate the neutron flux at the activation foil (black circle) from the *i*-th toroidal volume of emissivity ε_i (in light blue). The distance between each fractional volume ΔV_i (in purple) is $d_{i,j}$. The dark blue region does not contributed to the neutron flux at the activation foil as it is shadowed by the central column (light gray).

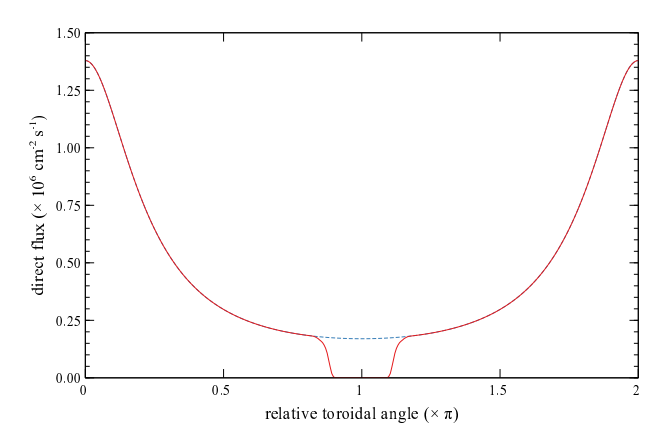


Figure 11 – Direct flux at the activation foil as a function of the toroidal angle φ with and without the effect of the central column shadowing (red and dashed blue curves respectively). The toroidal location of the AF has been located arbitrarily at $\varphi = 0$.

direct neutron flux $\langle \phi_{\mathrm{D},q} \rangle = \sum_m \phi_{\mathrm{D},q}(t_m)/M$ is used for the calculation of the time averaged activation rate R in the foil for plasma discharge as:

$$R_q = \alpha_q k \Gamma_q V \sum_{k=1}^K \Phi_{\mathrm{T}}(E_k) \Sigma(E_k) \eta(E_k)$$
 (2)

where V the activation foil volume, Γ_q the correction factor for the fast ion losses and redistribution, $\alpha_q = \langle \phi_{\mathrm{D},q} \rangle / \sum_k \Phi_{\mathrm{D}}(E_k)$ converts the MCNP neutron flux pulse height spectrum into an absolute neutron flux and $k \approx 0.65$ corrects for the over estimate of the fast ion population in TRANSP/NUBEAM due to the guiding center

approximation [27, 28]. This scaling factor has been confirmed by recent measurements of proton prompt losses [29]. The terms in the sum include $\Sigma(E_k)$, the macroscopic cross-section of the $^{115} {\rm In} + n \rightarrow ^{115m} {\rm In}$ reaction from TENDL [30], and $\eta(E_k)$ which takes into account the scattering and attenuation of neutrons in the activation foil itself. The index k runs over the energy bins of 50 keV width centered in E_k s in which the MCNP neutron flux pulse energy spectra shown in figure 9 have been calculated. The correction factor $\eta(E_k)$ has been calculated via MCNP simulations as the average of the ratio of the neutron flux (F4 tally) in four, 1 mm thick, cells representing the activation foil (see figure 12), to the primary neutron F4 tally from a mono-directional collimated source with a uniform energy distribution in the energy range 0 - 5 MeV (in the energy interval 1 to 3 MeV, $\eta=0.97$). The energy dependence of $\eta(E_n)$ shown in figure 12 shows an enhanced contribution to the flux at energies below to 2 MeV due to scattering in the activation foil and the suppression of the neutron flux at higher energies due to absorption. The expression in equation 2 is based on the assumptions

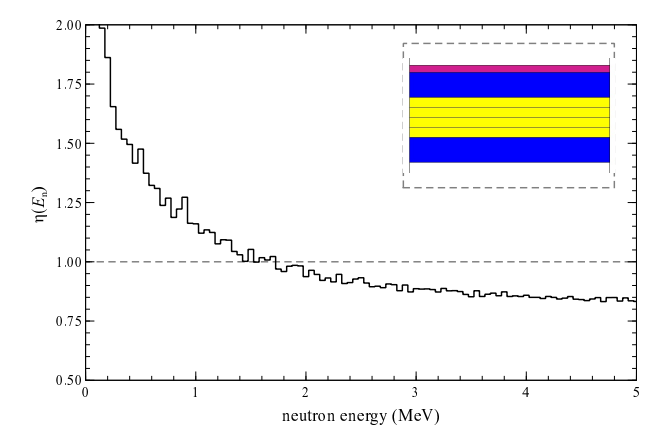


Figure 12 – Energy dependence of the correction factor η) to take into account scattering and attenuation of the neutrons in the activation foil calculated in MCNP as the average ratio of the neutron flux in the Indium foil to the primary neutrons. The inserts shows the AF's simplified cross-sectional geometry: in dark purple the stainless steel flange facing the plasma, in blue the plastic container and in the yellow the Indium activation foil.

that the burn-up is negligible (correct to a very good approximation), the foil is so thin that the flux is not perturbed (this is incorrect but already taken into account by the coefficient η) and that the neutron flux is constant: this is clearly incorrect as shown in figure 3, however, since the irradiation phase is much shorter than the half-life of the $^{115m}\text{In} \rightarrow ^{115}\text{In} + \gamma$ decay the number of activated nuclei N is proportional to average value of the rate.

3.4. Expected number of γ -rays counts on the detector

During an experimental day, a sequence of Q irradiation and decay phases follow each other. The irradiation in each plasma discharge q lasts $\tau_q = t_{\mathrm{e},q} - t_{\mathrm{s},q}$ where the indexes "s" and "e" indicate the start and end times of the NBI phase (for q = 1, $t_{\mathrm{s},1} = 0$ and $N(t_{\mathrm{s},1}) = 0$). The number of activated radionuclides at the end of the

irradiation phase of pulse Q is given by:

$$N(t_{e,Q}) = \frac{R_Q}{\lambda} \left[1 - e^{-\lambda \tau_Q} \right] + \sum_{q=1}^{Q-1} \frac{R_q}{\lambda} \left[1 - e^{-\lambda \tau_q} \right] e^{-\lambda (t_{e,Q} - t_{e,q})}$$
(3)

where λ is the decay constant of the $^{115m}\text{In} \to ^{115}\text{In} + \gamma$ reaction. After this last pulse Q, the number of activated radionuclide decays according to:

$$N(t) = N(t_{e,Q})e^{-\lambda(t - t_{e,Q})}. (4)$$

The expected number of detected decays $N_{\rm D}$ in the time interval $\Delta t = t_2 - t_1$ following the last irradiation is then given by:

$$N_{\rm D} = \epsilon I_{\gamma} f N(t_1) \left[1 - e^{-\lambda \Delta t} \right] \tag{5}$$

where ϵ is the γ -rays detector efficiency, $I_{\gamma}=0.46$ the branching ratio (γ -ray per disintegration) and f=0.91 the self-attenuation of the γ -rays in the activation foil which has been calculated by MCNP using the same geometry for the activation foil shown in figure 12 using a mono-directional photon source with an energy of $E_{\gamma}=336$ keV. The expected number of detected decays $N_{\rm D}$ will be compared in the next section to the experimental observations reported in table 1 in column under the heading "peak area". The population of the 115m In state due to energetic γ -rays from run-away electrons is not taken into account in this work. Observation of runaway electrons in MAST Upgrade is limited to plasma scenarios characterized by very low density not representative of the plasma scenarios of this study: in such plasmas, runaway-electrons are emitted at the very end of the plasma discharge and thus of limited importance. In addition, the cross-section for the 115 In $(\gamma, \gamma')^{115m}$ In reaction is approximately a factor 100 smaller than the one for the 115 In $(n, n')^{115m}$ In and it has an energy threshold of 8 MeV.

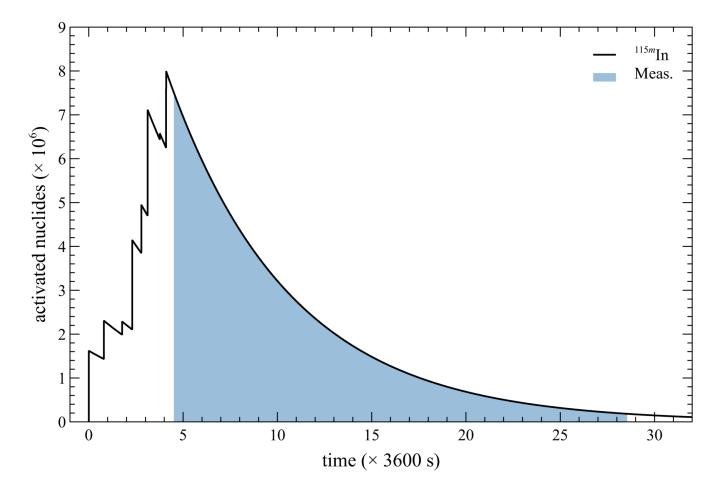


Figure 13 – Time evolution of the activated radionuclides for the MU01 AF exposure on the 08-10-21. The vertical steps indicate the activation for each plasma discharge. In pale blues, the time interval in which the expected number of decays is calculated.

3.5. Uncertainties in the modeling

The expected number of counts measured by the γ -rays detector calculated using equations 2 and 5 depend on several parameters and quantities whose uncertainties are reviewed in this section. To begin with, the following quantities are assumed to have a negligible errors: the AF foil volume V, the correction factors η and f, the decay constant λ and the branching ratio I_{γ} . The macroscopic cross-section Σ has a relative uncertainty of 10 % in the energy range of interest as determined in the TENDL database. The relative uncertainty in the integral total neutron flux from MCNP simulation is less than 2 % while the relative uncertainty in the TRANSP/NUBEAM predicted direct neutron flux $\langle \phi_{\mathrm{D},q} \rangle$ is the combination of a 10 % relative uncertainty in the neutron emissivity $\varepsilon(t_m)$, due to the uncertainty in the kinetic profiles and in Z_{eff} , and the standard error of the average $\langle \phi_{\mathrm{D},q} \rangle$ for the q-th plasma discharge. The uncertainty in the factor k is ± 0.05 as described in [27]. As a result, the overall relative uncertainty in α_q varies between 5 % to 25 % depending on the plasma discharge. Finally, the relative uncertainty in the detector efficiency is 8 % (see section 2).

4. Results and discussion

Good agreement is found between modeled and experimental number of counts in the γ -rays detector for all the analyzed experimental days as shown in Table 3 with the exception of the data for the 20-10-23 due to unreliable TS data. It is also interesting to note that the other prediction that deviates most from the measurements is for MU01 for which the energy fractions of the on-axis NBI had to be inferred from spectroscopic measurements (see section 3.1): the result here obtained suggests that the full energy component might have been slightly over estimated. Nevertheless, the best estimate of the ratio $N_{\rm E}/N_{\rm D}$ provided by the weighted average of the five measurements is 1.0 ± 0.1 . The large uncertainty in $N_{\rm D}$ mainly reflects the uncertainties in the kinetic profiles in input to TRANSP/NUBEAM and the large fluctuation of the neutron flux at the detector in a single discharge. The most critical parameter in this study is

	_	(5\	I == / 5\	
Exp .	Date	$N_{\rm E}~(\times 10^5)$	$N_{\rm D}~(\times 10^5)$	ratio
MU01	08-20-21	1.74 ± 0.001	1.97 ± 0.38	0.88 ± 0.18
MU02	26-01-23	2.94 ± 0.013	2.97 ± 0.62	0.99 ± 0.20
MU02	27-01-23	1.95 ± 0.001	2.09 ± 0.43	0.93 ± 0.19
MU03	20-10-23	2.20 ± 0.001	1.62 ± 0.34	1.36 ± 0.27
MU03	27-10-23	4.03 ± 0.020	3.96 ± 0.88	1.01 ± 0.21

Table 3 – Comparison between the modeled $N_{\rm D}$ and the measured $N_{\rm E}$ counts on the γ -rays detector after irradiation of the activation foil for the selected experimental days.

the estimate of the reduction in the neutron emissivity due to the redistribution and loss of fast ions resulting from resonant and non-resonant perturbation. In order to eliminate this problem, it is suggested that future activation foil measurements should be carried out in dedicated experiments in which no or minimal magnetic perturbations are present. Luckily, this can be easily achieved in MAST Upgrade in L-mode plasmas in double null, conventional divertor configuration by using only the off-axis NBI as it has been shown that resonant perturbations are absents and non-resonant ones are very week and not affecting the fast ions. Internal reconnection events, which cause massive ejection of fast ions from the plasma core with almost

complete neutron production suppression, typically occur in the ramp-up phase or at the very beginning of the plasma current flat top phase could be easily avoided by late neutral beam injection. An example of suitable plasma discharge that matches the requirements above and that can be used as the reference scenario is shown in figure 14. The measured magnetic perturbation with the Mirnov OMAHA coil is practically zero (compared with the 2nd panel from bottom of figure 7) and the neutron rate measured by the FC (suitably scaled) matches the one predicted by TRANSP for the entire plasma discharge.

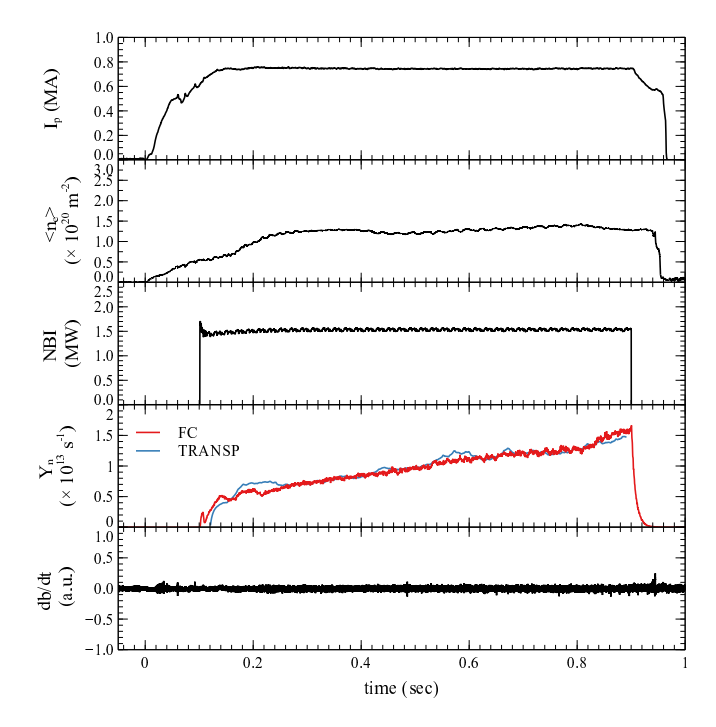


Figure 14 – Example of a plasma discharge (# 47119) with off-axis NBI heating only ideal for activation foil measurements characterized by the lack of resonant and non-resonant perturbations causing the redistribution and loss of fast ions. The bottom panel of this figure can be compared with the 2nd panel from bottom of figure 7.

The agreement between $N_{\rm D}$ and $N_{\rm E}$ obtained with the forward modeling presented in this paper can then be used to absolutely calibrate the FC against the TRANSP/NUBEAM predicted neutron rate as well as to assess the validity of the kinetic profiles and the external auxiliary heating power in input to the models. These results support the idea that forward modeling of the AF can lead to an accurately estimate of the neutron yield and therefore potentially being used as calibration procedure for ITER, DEMO and future fusion power plants as suggested in [31, 32]. In addition, for a fusion reactor, the reference plasma scenarios will be characterized by a neutron emissivity dominated by the thermal component from the DD and DT reactions thus simplifying significantly the forward modeling effort.

Acknowledgments

This work has been carried out within the framework of the EUROfusion Consortium, funded by the European Union via the Euratom Research and Training Programme (Grant Agreement No. 101052200 - EUROfusion). Views and opinions expressed are, however, those of the author(s) only and do not necessarily reflect those of the European Union or the European Commission. Neither the European Union nor the European Commission can be held responsible for them. This work has been carried out with the support of the RCUK Energy Programme (Grant No. EP/T012250/1) and of the Swedish Research Council (VR) Grant No. 2021-05485.

References

- [1] Hendel H W et al. 1990 Rev. Sci. Instrum. 61 1900-1914
- [2] Strachan J D, et al. 1990 Rev. Sci. Instrum. 61 3501–3504
- [3] Nishitani T et al. 1992 Rev. Sci. Instrum. 63 5270–5278
- [4] Jassby D L et al. 1995 Rev. Sci. Instrum. 66 891–893
- [5] Sasao M et al. 2010 Rev. Sci. Instrum. 81 10D329
- [6] Nishio N et al. 2011 Plasma and Fusion Research 6 2405115-2405115
- [7] Syme D et al. 2014 Fus. Eng. Design 89 2766–2775
- [8] Batistoni P et al. 2018 Nucl. Fusion 58 026012
- [9] Batistoni P et al. 2018 Nucl. Fusion 58 106016
- [10] Snoj L, et al. 2012 Fus. Eng. Design 87 1846–1852
- [11] Ishikawa M et al. 2013 Fus. Eng. Design 88 1377–1381
- [12] Bertalot L et al. 1999 Rev. Sci. Instrum. 70 1137–1140
- 13 Chae S et al. 2021 Nucl. Eng. Technology **53** 3012–3017
- [14] Hoek M et al. 1996 Nucl. Instrum. Methods A 368 804-814
- [15] Prokopowicz R et al. 2011 Nucl. Instrum. Methods A 637 119–127
- [16] Stankunas G et al. 2015 Nucl. Instrum. Methods A **788** 168–172
- [17] Goldston R J et al. 1981 J. Comput. Phys 43 61
- [18] Pankin A et al. 2004 Commun. Comput. Phys. 159 157
- [19] Cecconello M $et\ al.\ 2018\ Rev.\ Sci.\ Instrum.\ \ {\bf 89}\ 10I110$
- [20] Cecconello M et al. 2023 Plasma Phys. Control. Fusion 65 035013
- [21] Goorley J T 2014 MCNP 6.1.1 Beta Release Notes Tech. Rep. LA-UR-14-24680 Los Alamos National Laboratory
- [22] Conway N J et al. 2010 Rev. Sci. Instrum. 81 10D738
- [23] Gibson K et al. 2010 Plasma Phys. Control. Fusion 52 124041
- [24] McClements K G et al. 2012 Phys. Plasmas 19 072514
- [25] Zankl G et al. 1981 Nucl. Instrum. Methods 185 321–329
- [26] Wolle B et al. 1999 Nucl. Instrum. Methods A 424 561–568
- [27] Cecconello M et al. 2019 Nucl. Fusion 59 016006
- [28] Sperduti A et al. 2021 Nucl. Fusion 61 016028
- [29] Aboutalb A et al. 2024 Rev. Sci. Instrum. Accepted for Publication
- [30] Koning A J et al. 2019 Nuclear Data Sheets 155 1
- [31] Cecconello M et al. 2019 Fus. Eng. Design 146 2049–2052
- [32] Cecconello M et al. 2019 JINST 14 C09001